



## Research Paper

Combination of photoelectrocatalysis and adsorption for removal of bisphenol A over TiO<sub>2</sub>-graphene hydrogel with 3D network structureYu Zhang<sup>a</sup>, Wenquan Cui<sup>a,\*</sup>, Weijia An<sup>a</sup>, Li Liu<sup>a</sup>, Yinghua Liang<sup>a</sup>, Yongfa Zhu<sup>b,\*</sup><sup>a</sup> College of Chemical Engineering, Hebei Key Laboratory for Environment Photocatalytic and Electrocatalytic Materials, North China University of Science and Technology, Tangshan Hebei 063210, PR China<sup>b</sup> Department of Chemistry, Tsinghua University, Beijing 100084, China

## ARTICLE INFO

**Keywords:**  
 TiO<sub>2</sub>-graphene hydrogel  
 3D structure  
 Adsorption-photoelectrocatalysis  
 BPA removal

## ABSTRACT

We successfully fabricated the three-dimensional (3D) hydrogel of titanium dioxide (TiO<sub>2</sub>)-graphene using a simple one-pot method and exhibited enriched adsorption-photoelectrocatalytic degradation ability of low-concentration bisphenol A (BPA). Combined with the unique adsorption of graphene hydrogel and the effective photoelectrocatalytic performance of TiO<sub>2</sub>, we rapidly enriched the organic pollutants and conducted efficient *in situ* degradation. The low-concentration BPA (20 mg/L) was degraded completely by the TiO<sub>2</sub>-rGH electrode in 5 h through the synergistic effect of adsorption-photoelectrocatalytic. The photogenerated charge on the surface of TiO<sub>2</sub> is rapidly separated by the action of the applied electric field and the graphene sheet. The high conductivity of the graphene makes the TiO<sub>2</sub>-graphene hydrogel rapidly conducting the charge and solves the problem of poor conductivity of the semiconductor electrode. On the basis of these advantages, the TiO<sub>2</sub>-rGH has a cross-porous network structure that favors the anchor of more TiO<sub>2</sub> nanocrystals, the specific surface area and reactive sites are greater than the thin film electrode, and the structure is conducive to significantly improving the BPA removal efficiency. By contrast, the BPA degradation of TiO<sub>2</sub>-rGO thin film electrode was 40% after 4 h of ultraviolet irradiation, whereas the removal rate of BPA over the same mass of TiO<sub>2</sub>-rGH electrode rate was up to 96%. At the same time, the TiO<sub>2</sub>-rGH electrode without filtering can be achieved quickly separated from the recovery due to its special macro-3D network structure. Its removal ability still maintains above 90% after 10 times cyclic experiments with self-regeneration characteristics. It can be achieved rapid separation and recovery without filtering.

## 1. Introduction

Economic development must be based on the development of resources and the transformation of the environment, which inevitably bring environmental pollution problems. With high toxicity, long-term residue and bioaccumulation of refractory organic pollutants are important problems caused by the current levels of environmental pollution [1–3]. For organic wastewater, the main treatment methods are adsorption method [4–7]. The adsorption capacity of the adsorbent with a large specific surface area and suitable pore structure is strong, but the method has the disadvantages of poor selectivity, small adsorption capacity, secondary pollution, and other issues. Electrocatalytic (EC) oxidation [8,9] has been a relatively widely used water treatment method in recent years. It has a good catalytic activity for refractory organic pollutants, but it is necessary to select an anode material with high catalytic activity and, in the process of electrolysis, to ensure its sustained high surface activity as well as the EC oxidation

of the existence of low-current efficiency, energy consumption, and other issues.

Since 1972, Fujishima and Honda found that titanium dioxide (TiO<sub>2</sub>) can photocatalytically decompose water [10]. Photocatalytic (PC) technology has been an issue of broad concerned in the field of the environmental pollution and new energy development. This technology is considered to be green, environmentally friendly, and to have a promising depth of water treatment technology [11]. The light catalyst represented by TiO<sub>2</sub> has high activity, low cost, stable physical and chemical properties, and nontoxic advantages, which often are used for the degradation of organic pollutants [12,13]. It poses some problems, however, such as a large band gap and low quantum efficiency. The suspension system also has many shortcomings: it is not conducive to recycling, and has a high cost, which hinders the practical use of this new technology.

Photoelectrocatalytic [14] (PEC) technology is a kind of catalytic oxidation technology that uses photoelectric synergistic technology. It

\* Corresponding authors.

E-mail addresses: [wk cui@163.com](mailto:wk cui@163.com) (W. Cui), [zhu yf@mail.tsinghua.edu.cn](mailto:zhu yf@mail.tsinghua.edu.cn) (Y. Zhu).

effectively suppresses the recombination of electron hole pairs, the degradation rate is fast and lacks selectivity, the energy consumption is small and lacks secondary pollution, and it offers easy separation and recovery. PEC has attracted great attention for not only water oxidation treatment but also hydrogen production from water splitting [15]. At present, the most widely used PEC technology is the thin film electrode [16], but its contact area is small and the active site is small. Wei et al. [17] examined PEC activities with different thicknesses of  $\text{TiO}_2\text{-gC}_3\text{N}_4$  film electrode and found that the photocurrent could reach the maximum value ( $I_p = 3.6 \mu\text{A}$ ) and determined that the PEC degradation activity is best with a thickness of  $1.5 \mu\text{m}$ . Therefore, increasing the visible active site and increasing the thickness of the electrode can decrease the electrode conductivity and the catalytic activity. The array electrode [18,19] is limited to the thickness of the film electrode and the increase of the active site. This finding reveals that PEC technology still poses many problems. First, we need to determine how to increase the electrode active sites without reducing conductivity. Second, if not prepared by anodic oxidation of the  $\text{TiO}_2$  electrode, the catalyst is easy to fall off the carrier, and the lack of a fixed effect also reduces the degradation efficiency of the catalyst. Therefore, it is necessary to improve the fixed effect and increase surface area methods.

In contrast to other materials, graphene is a more attractive support material for nanoparticle loading. Its high surface area [20], high electron mobility [21], good mechanical strength [22], and optical properties [23], have attracted increasing attention, making it extensively studied in many research fields, including, for example, its high surface area and strong adsorption ability based on the design of many effective adsorbents [24,25] and photocatalysts [26–28] for removal and PC degradation of pollutants. In addition, graphene's excellent conductive properties based on earlier research for the electrode has its composite, Fan [29] using chemical vapor deposition(CVD) prepared a three-dimensional (3D) sandwich structure of a graphene–carbon nanotube composite material with a modified electrode and found that the capacitance could be as high as  $385 \text{ F/g}$ . Choi [30] also used CVD to prepare a graphene composite electrode for a dye-sensitized solar cell, wherein the photoelectric conversion efficiency of dye sensitized solar cells in graphene was 4.46%. Graphene, which has good conductivity and good mechanical properties, is considered to be the most promising electrode material [31].

We combined the 3D graphene hydrogel (rGH) system and  $\text{TiO}_2$  to form a  $\text{TiO}_2\text{-rGH}$  with a 3D network structure and applied it to the degradation of organic pollutants using adsorption-photoelectrocatalysis. Graphite oxide (GO) and  $\text{TiO}_2$  are formed by stacking the graphene sheet to form a 3D structure. Graphene's internal through-hole structure and high conductivity can effectively suppress the problem of slow charge transfer because of the increase in electrode thickness. Because of the  $\text{TiO}_2$  nanocrystals anchored to the 3D graphene sheet, the photogenerated charge can be transferred quickly to the graphene layer, effectively promote the separation of photo-generated electron-hole pairs, and improve the active sites. In the process of degradation, graphene has high specific surface area and effective product enrichment. At the same time, to achieve efficient adsorption and in situ PEC synergistic degradation, it can target pollutants that are completely degraded by PEC oxidation of  $\text{TiO}_2$  with high efficiency. This work provides new insights into the fabrication of hydrogel-based materials and facilitates their potential application for the removal of various aquatic pollutants of water purification.

## 2. Experimental methods

### 2.1. Preparation of graphite oxide

All the reagents used were of analytical grade and were used without further purification. GO was prepared following Hummers' method [32] with little improvement. Three grams of graphite were added to a 70-mL sulfuric acid (98 wt%) ice bath, which was stirred

continuously for 10 min. Then 1.5 g of sodium nitrate and 9 g of potassium permanganate were added successively, and the resultant mixture was maintained in a continuous ice bath and stirred for 2.5 h. The system then was heated to 308 K for 3.5 h, and 150 mL of deionized water was added carefully. The system temperature then increased to 368 K and was stirred continuously for 1.5 h. Next, 300 mL of deionized water and 20 mL of hydrogen peroxide (30%) were added successively. The reaction product was washed several times with 1:10 diluted hydrochloric acid under 4800 rpm centrifugation for 40 min. The aqueous solution of GO was obtained 7 days after dialysis with MD44 (3500D) dialysis membranes.

### 2.2. Preparation of a $\text{TiO}_2\text{-rGH}$ with a 3D network structure

$\text{TiO}_2$  and 0.5 mL of polyethylene glycol 200 were ground, and after 5 min, a constant amount of GO was added. The grinding continued for 5 min to ensure that the  $\text{TiO}_2$  and GO were mixed thoroughly. The  $\text{TiO}_2$  and GO were prepared in different proportions of  $\text{TiO}_2$  and GO with mass ratios of 1:4, 2:3, 3:2, and 4:1, respectively. The mixture was treated in an ultrasonication bath for 60 min. Then, a 10-fold amount of GO relative to ascorbic acid (VC) was added and ultrasonication continued for an additional 30 min. To obtain the  $\text{TiO}_2\text{-rGH}$  electrode, 1 mL of this mixed solution was placed in a self-made polytetrafluoroethylene reaction mold with a  $2 \times 2.5 \text{ cm}$  titanium mesh with a pore size of  $178 \mu\text{m}$ , and the solution was kept at 368 K for 60 min. The resulting electrode was immersed in deionized water to remove the unreacted VC. The specific  $\text{TiO}_2\text{-rGH}$  electrode formation process is shown in Fig. 1. The  $\text{TiO}_2\text{-rGH}$  electrode formed by a simple one-pot method mainly undergoes the following stages: (1)  $\text{TiO}_2$  and GO are mixed thoroughly by grinding and ultrasound; (2) the mixed solution is placed in a mold with titanium mesh; and (3) the  $\text{TiO}_2\text{-rGH}$  electrode is obtained by reducing the VC at 368 K using the hydrophobicity of the graphene sheet and the  $\pi$ - $\pi$  conjugation effect. The electrode was washed with distilled water to remove unreacted VC.

### 2.3. Preparation of $\text{TiO}_2\text{-rGO}$ thin film

The  $\text{TiO}_2\text{-rGO}$  thin film was prepared according to the thin film electrode preparation method by Zhen [17]. Specifically, a  $\text{TiO}_2$  and GO mixed solution was created and reacted for hours in an ultrasonic bath. Then, a 10-fold excess of GO relative to VC was added and the ultrasound treatment continued for 30 min. The indium tin oxides (ITO) glass then was immersed in the mixed solution. The typical dip-coating process parameters are as follows: lifting height of 2 cm, dip time of 60 s, and impregnation pulling speed for  $50 \mu\text{m/s}$ . After completing these steps three times, the electrodes were dried at 353 K for 1 h and the catalyst was obtained on the ITO electrode. As a control, the  $\text{TiO}_2$ -activated carbon (AC) thin film electrodes were prepared by the same procedure. The mass ratio of  $\text{TiO}_2$  and GO (and  $\text{TiO}_2$  and AC) were both 4:1.

### 2.4. Characterization

The microstructure of the material was observed by scanning electron microscopy (SEM) using a Hitachi S-4800 (Tokyo, Japan) field emission SEM. A JEOL JEM-2100F (Tokyo, Japan) field emission transmission electron microscope (TEM) was used for TEM and high-resolution TEM (HRTEM). The samples were subjected to phase analysis

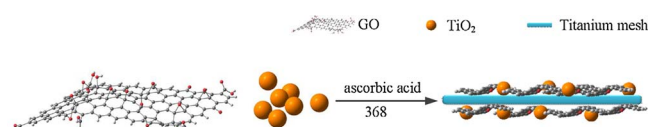


Fig. 1. Schematic of the preparation process of  $\text{TiO}_2\text{-rGH}$  electrode.

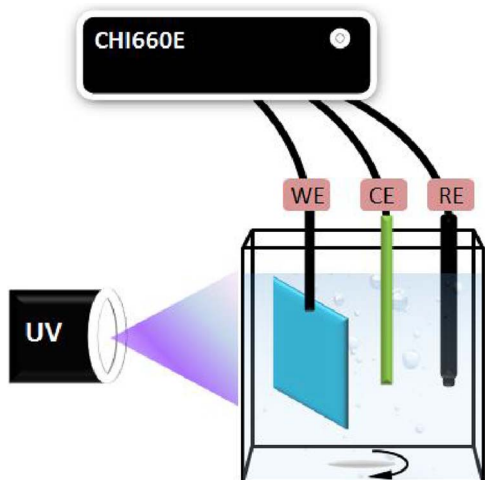


Fig. 2. Schematic of the PEC system setup with working electrode (WE), Pt counter electrode (CE), saturated calomel electrode (RE).

using a Rigaku D/MAX2500PC (Tokyo, Japan) x-ray diffractometer (XRD) with a working voltage of 40 kV, a working current of 100 mA, and a scanning range of 5°–80°. The molecular structure of the samples was analyzed using Thermo Nicolet Avatar 370 (Waltham, MA) Fourier transform infrared (FTIR) spectroscopy. The atomic structure and electronic properties were determined using a Thermo Scientific™ DXR™ (Waltham, MA) laser Raman spectrometer (Raman) with 524-nm excitation. The radicals of the catalyst were measured using a JEOL JES-FA200 electron spin resonance (ESR) spectrometer.

### 2.5. Photoelectric performance test

The PEC test used the CHI 660E (Shanghai, China) electrochemical system workstation as shown in Fig. 2. The reaction also was performed in a three-electrode battery system using 0.1 M sodium sulfate ( $\text{Na}_2\text{SO}_4$ ) as an electrolyte solution while immersing the electrode in 2 cm of the solution. A platinum (Pt) wire (length 70 mm and diameter 0.4 mm) was used as a counter electrode and a saturated calomel electrode (SCE) was used as the reference electrode. A mercury lamp with a total luminous output of 15 W (model: CEL-M500) was placed 10 cm in front of the electrode.

### 2.6. Static adsorption

Different proportions of electrodes were prepared on a cubic ( $5 \times 5 \times 5$  cm) quartz glass reactor and 100 mL 20 mg/L of bisphenol A (BPA) was added. A temperature of  $298 \pm 2$  K was held and the stirring speed was 200 r/min. The solution was sampled every 30 min (1 mL) after filtration with a 0.45  $\mu\text{m}$  filter. The BPA concentration was determined using a Hitachi high-performance liquid chromatograph (HPLC).

### 2.7. PC, EC, and PEC degradation of BPA

For comparison, PC, EC, and PEC degradation experiments were performed under the same conditions as in Section 2.5. Notably, the concentration of  $\text{Na}_2\text{SO}_4$  was 150 mg/L. Every 30 min, 1 mL of the solution was filtered with a 0.45  $\mu\text{m}$  filter. The BPA concentration was determined by HPLC.

## 3. Results and discussion

### 3.1. Morphology and phase characterization of a $\text{TiO}_2$ -rGH

Fig. 3 shows the SEM images and digital pictures of  $\text{TiO}_2$ -rGH and

$\text{TiO}_2$ -rGO thin film electrode. Fig. 3a is the micrograph of rGH. It is evident that rGH has a well-defined and interconnected 3D pore structure with pore sizes ranging from several micrometers to several nanometers, mainly micron-sized pores; the formation of these morphologies mainly is due to the hydrophobic interaction between the graphene sheets after reduction,  $\pi$ - $\pi$  conjugation, and intermolecular forces [33]. From Fig. 3b, it is evident that the  $\text{TiO}_2$ -rGH adheres well to the titanium wire, and the diameter of the titanium wire is about 100  $\mu\text{m}$ . The uneven structure of the surface is the main reason the  $\text{TiO}_2$ -rGH can be attached to the titanium mesh. Although the rGH has a 3D pore structure, Fig. 3a shows the accumulation of graphene sheets. Fig. 3c and d shows that the pore size of  $\text{TiO}_2$  and rGH composite is reduced obviously, which indicates that  $\text{TiO}_2$  nanoparticles can inhibit the agglomeration of graphene lamellae. It is clear from the inset of Fig. 3d that  $\text{TiO}_2$  is distributed evenly in the 3D network of rGH, and it is proved that graphene also has the effect of promoting the dispersion of  $\text{TiO}_2$ . The existence of this close contact mechanism between graphene and  $\text{TiO}_2$  is beneficial to the photogenerated charge transfer between  $\text{TiO}_2$  and graphene sheets, which provides macroscopic evidence for the possible existence of chemical bonds between  $\text{TiO}_2$  and graphene. Fig. 3e and f shows SEM of the  $\text{TiO}_2$ -rGO thin film electrode. It is evident that the surface of the thin film electrode is uneven, but there is no pore structure. The ITO substrate makes close contact, which is conducive to charge conduction.

Fig. 3g is the left view of the  $\text{TiO}_2$ -rGH electrode. The figure shows that the macroscopic thickness of the  $\text{TiO}_2$ -rGH electrode is about 2 mm, and the thickness of the thin film electrode is only 3  $\mu\text{m}$  from the electron microscope (Fig. 3f). The results show that the  $\text{TiO}_2$ -rGH electrode has a developed 3D network structure, which provides more active sites for the later activity measurement. Because of the presence of graphene, the  $\text{TiO}_2$  nanoparticles are evenly distributed in the 3D network of graphene, and hence one can see that the prepared  $\text{TiO}_2$ -rGH electrode increases the electrode thickness to increase the active site and does not affect its conductivity. Fig. 3h is a physical diagram of titanium mesh and the  $\text{TiO}_2$ -rGH electrode. The figure shows that the diameter of the titanium mesh is 0.178 mm and the  $\text{TiO}_2$ -rGH can be well attached to the titanium mesh.

Fig. 4 shows the TEM and HRTEM of the rGH,  $\text{TiO}_2$ , and  $\text{TiO}_2$ -rGH. From Fig. 4a, the graphene layer in the hydrogel is almost transparent and has wrinkles. Fig. 4b shows the  $\text{TiO}_2$  nanoparticles; the nanoparticle size is about 20 nm and the pure titanium dioxide agglomeration is particularly serious. Fig. 4c is the TEM of the  $\text{TiO}_2$ -rGH. It can be seen from the image that the  $\text{TiO}_2$  nanoparticles are more evenly distributed on the graphene layer, and graphene effectively inhibit the agglomeration of  $\text{TiO}_2$ . The close contact between  $\text{TiO}_2$  and the graphene sheet is conducive to the transmission of photogenerated charge in Fig. 4d, which can effectively solve the poor conductivity of thin film electrode. The lattice spacing of the nanocrystals is 0.24 nm, corresponding to the (004) crystallographic plane of anatase phase of  $\text{TiO}_2$ , corresponding to the JCPDS card no. 21-1272 [34].

Fig. 5a is the XRD pattern of GO, rGH,  $\text{TiO}_2$ -rGH, and  $\text{TiO}_2$ . The characteristic peaks of GO are mainly in a sharp single peak at 12.282°, corresponding to the GO layer spacing of 0.72 nm. Compared with the graphite layer spacing of 0.34 nm [35], this spacing shows the phenomenon of expansion. The phenomenon of expansion is due to the introduction of a large number of oxygen-containing functional groups after the oxidation of the graphite, which results in the significant expansion of the lamellae of the graphite layer. By comparing rGH to GO, a new wide characteristic peak is evident at 24.7°. The corresponding rGH layer spacing is 0.36 nm, which is much smaller than the layer spacing of GO but close to the layer spacing of graphite. This spacing is due to the  $\pi$ - $\pi$  conjugation of the graphene sheet and the residual small oxygen-containing functional groups [36]. In the XRD spectrum of  $\text{TiO}_2$ ,  $\text{TiO}_2$  (P25) demonstrates two kinds of phases: an anatase phase and a rutile phase. The characteristic peaks appear at 25.3°, 36.9°, 37.8°, 38.6°, 48.0°, 53.9°, 55.1°, 62.7°, 68.9°, 70.3°, and 75.0° are

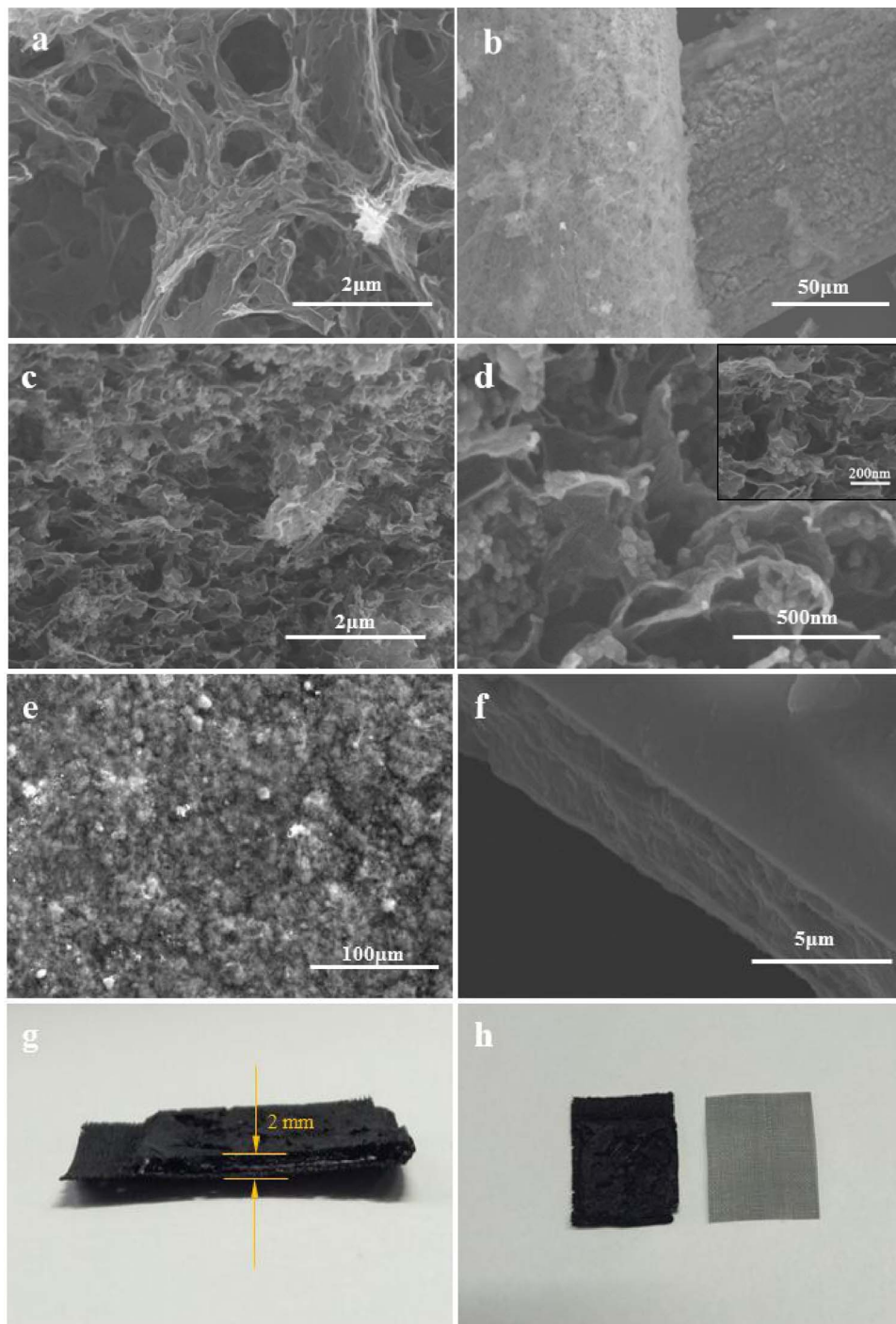
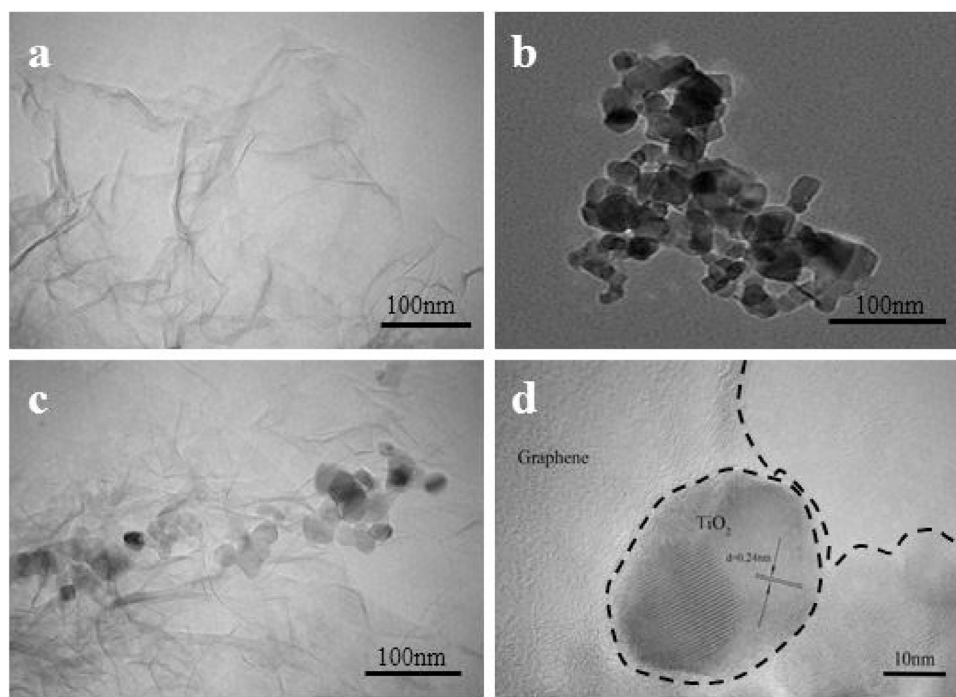


**Fig. 3.** SEM images of (a) rGH, (b, c, d) TiO<sub>2</sub>-rGH, (e, f) TiO<sub>2</sub>-rGO thin film electrode, (g, h) digital pictures of titanium mesh and TiO<sub>2</sub>-rGH.

ascribed to (101), (103), (004), (112), (200), (105), (211), (204), (116), (220), and (215) crystallographic planes of the anatase phase (JCPDS#65-5714), respectively; and the diffraction peaks appear at 27.5° and 36.0° are ascribed to the (110) and (101) crystallographic planes of the rutile phase (JCPDS#65-1119), respectively. The rGH characteristic broad spectrum appears at 24.5° for the TiO<sub>2</sub>-rGH sample, but it narrows obviously with respect to the peak width of GO. The nano-TiO<sub>2</sub> (P25) was successfully compounded with rGH, and chemical bonds might exist between them.

Fig. 5b shows the FTIR spectrum of TiO<sub>2</sub>, GO, and TiO<sub>2</sub>-rGH. A wide and strong absorption peak appears at 3420 cm<sup>-1</sup> in the FTIR graph for GO, which belongs to the stretching vibration absorption peak of O—H. The stretching vibration absorption peak of carbonyl C=O appears at

1726 cm<sup>-1</sup>, the skeleton vibration absorption peak of C=C appears at 1623 cm<sup>-1</sup>, and the bending vibration absorption peak [37] of C—H appears at 1400 cm<sup>-1</sup>. After reduction of VC, the absorption peaks of the oxygen groups in the FTIR of TiO<sub>2</sub>-rGH are weakened, and the absorption peaks of the carbonyl C=O disappear, which indicates that a large number of oxygen-containing groups are reduced, although some oxygen-containing groups still are retained. Comparison of XRD, the oxygen-containing functional groups introduced were consistent. A significant Ti—O—Ti absorption peak appears at 670 cm<sup>-1</sup> in the FTIR picture of TiO<sub>2</sub>, and it is obvious that the Ti—O—Ti absorption peak is obviously weakened in TiO<sub>2</sub>-rGH, and a small peak appears at 798 cm<sup>-1</sup>, which may be Ti—O—C peak [38]. This proves that an interaction may exist between TiO<sub>2</sub> and rGH, which is consistent with the



#### XRD results.

Raman spectroscopy can be used to identify the difference between single-layer and double-layer graphene, and graphite thin-layer and bulk graphite. Fig. 6 shows the Raman spectra of GO, rGH, TiO<sub>2</sub>-rGH, and TiO<sub>2</sub>. The D, G, and 2D peaks are the three most important graphene characteristic peaks, and the D peak near 1350 cm<sup>-1</sup> is the defect peak, that is, the number of defects or the edge of the reaction graphite layer. The G peak near 1580 cm<sup>-1</sup> is the characteristic peak of sp<sup>2</sup> hybrid carbon atoms, which reacts with its symmetry and crystallinity. The 2D peaks near 2700 cm<sup>-1</sup> are derived from two-phonon inelastic scattering [39], which can be used as a characteristic peak to identify the graphene and graphite. The intensity ratio of the D peak and G peak is used to measure the degree of disorder and the degree of reduction of the conjugated plane of I<sub>D</sub>/I<sub>G</sub>. It can be seen from the Raman diagram that the I<sub>D</sub>/I<sub>G</sub> of rGH is significantly higher than that of the GO, indicating that the carbon atoms and oxidized molecular defects of sp<sup>2</sup> are reduced significantly [40]; the I<sub>D</sub>/I<sub>G</sub> of TiO<sub>2</sub>-rGH is similar to rGH. The TiO<sub>2</sub> Raman vibration peaks appear in the Raman spectra of TiO<sub>2</sub>-rGH, and the corresponding vibration modes are all anatase characteristic vibration peaks [41] at 388, 495, and 620 cm<sup>-1</sup>.

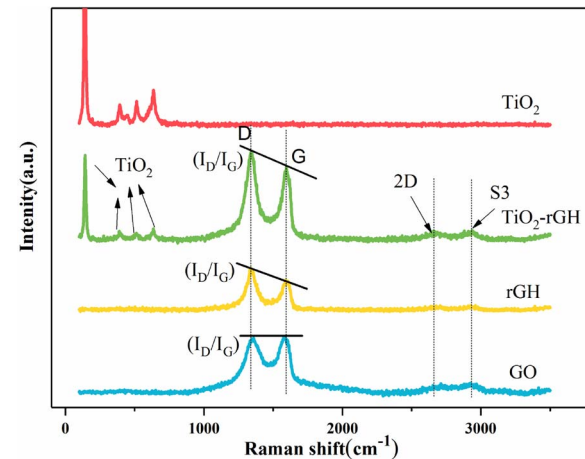


Fig. 6. Raman spectra of GO, rGH, TiO<sub>2</sub>-rGH, and TiO<sub>2</sub>.

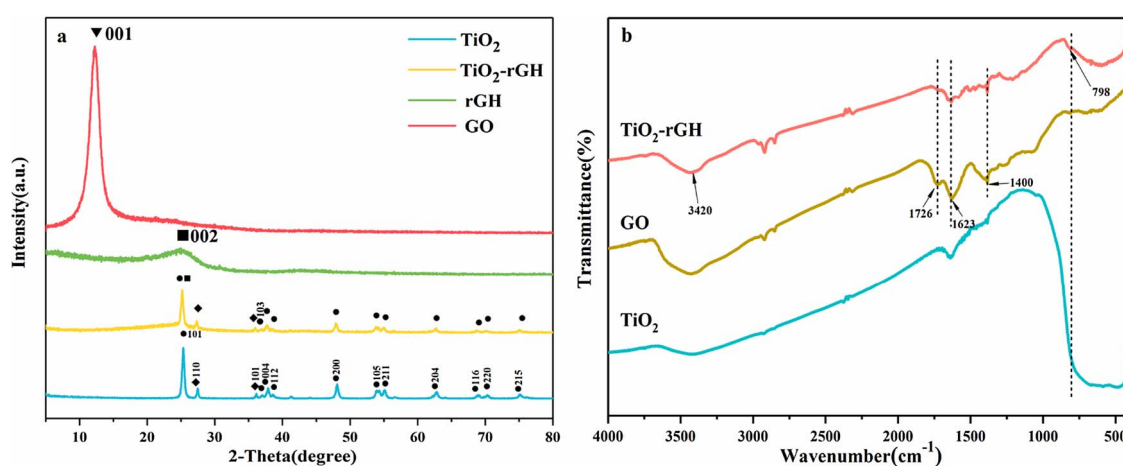


Fig. 5. (a) XRD spectra of GO, rGH, TiO<sub>2</sub>-rGH, and TiO<sub>2</sub>; (b) FTIR spectra of TiO<sub>2</sub>, GO, and TiO<sub>2</sub>-rGH.

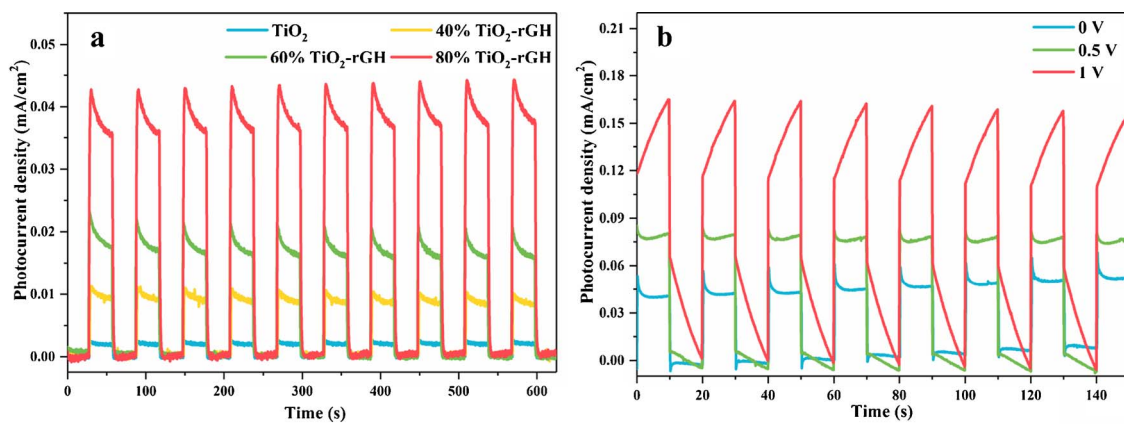


Fig. 7. (a) Amperometric photocurrent responses of TiO<sub>2</sub> and different mass ratio TiO<sub>2</sub>-rGHS in 0.5 M Na<sub>2</sub>SO<sub>4</sub> electrolyte solution. (b) Amperometric photocurrent responses of 80% TiO<sub>2</sub>-rGH at 0, 0.5, and 1 V in 0.5 M Na<sub>2</sub>SO<sub>4</sub> electrolyte solution.

It is evident that both the D and G peaks increase after TiO<sub>2</sub> and rGH complexes, indicating that the sp<sup>2</sup> hybrid carbon atom structure increases and the TiO<sub>2</sub> has a weak Raman enhancement effect [42]. These results are due to the effective electron transfer between graphene and TiO<sub>2</sub>.

The transient photocurrent response is a direct indication of the photoresponsive response. From Fig. 7a, the maximum photocurrent density of the 80% TiO<sub>2</sub>-rGH is 0.042 mA/cm<sup>2</sup> when the external bias voltage is 0 V and the light area is 4 cm<sup>2</sup>. The switching lamp leads to the transient response of the photocurrent. The photocurrent of the sample increases with an increase in the TiO<sub>2</sub> content, but in contrast, the photocurrent of pure TiO<sub>2</sub> is almost invisible, which objectively reflects the existence of a high concentration of the electron-hole complex and the low quantum efficiency problems of TiO<sub>2</sub>. When TiO<sub>2</sub> and graphene were combined, the high-charge mobility of graphene and the pore structure inside the hydrogel were fully utilized to promote the separation of the TiO<sub>2</sub> electron-hole pairs and to improve the photocurrent. In addition, when the 0.5 V and 1 V bias voltage is applied to the electrode (Fig. 7b), the photocurrent density is up to 0.128 mA/cm<sup>2</sup>, which is three times that of the TiO<sub>2</sub>-rGH without bias. Therefore, the external bias voltage can effectively transfer the photo-generated electrons to the counter electrode. The presence of graphene gives the TGH a high conductivity, further promotes the separation of the electron-hole pairs, and improves the photoelectric response. These results indicate that the TiO<sub>2</sub>-rGHS exhibit excellent photoelectric properties and stability.

Electrochemical impedance spectroscopy (EIS) is a powerful tool used to study the interfacial properties between the electrode and the

solution by measuring the variation of impedance with the sine wave frequency. The EIS measurements are made at intervals of 1 × 10<sup>5</sup>–0.1 Hz. Fig. 8a shows the Nyquist plot of the TiO<sub>2</sub>-rGHS under dark and ultraviolet (UV) irradiation. The internal enlargement diagram shows the equivalent circuit of the impedance spectrum fitted with the ZSimpWin software to further analyze the EIS. R<sub>1</sub> represents the series resistance of the system, R<sub>2</sub> represents the semiconductor loss resistance (space charge) layer, R<sub>3</sub> represents the charge transfer at the Helmholtz layer, and CPE represents the chemical capacitance [43].

The radius of the circle of the TiO<sub>2</sub>-rGH with the light on is much smaller than the radius of the circle in the dark reaction. From the data in Table 1, it is evident that the R<sub>3</sub> (3308 Ω) of the dark reaction is significantly larger than R<sub>3</sub> (784.4 Ω) after turning on the light, and the radius of the circle is further reduced at 1 V bias. The values of R<sub>3</sub> are less than 100 after 1 V bias, which indicates that having the light on and the external bias both can promote the charge transfer and reduce the electron-hole recombination rate. Fig. 8b shows the cyclic voltammograms of the TiO<sub>2</sub>-rGH at different sweep speeds. On the basis of these findings, we added 20 mg/L BPA to the photoelectric measurement system. It is evident that the oxidation potential of BPA is 0.5 V and a good linear relationship exists between the peak current and the sweep speed, which proves that BPA is controlled by the surface of the TiO<sub>2</sub>-rGH [44].

We conducted linear sweep voltammetry in a three-electrode system. The TiO<sub>2</sub>-rGH electrode was the working electrode, the SCE and the platinum wire were the reference electrode and the counter electrode, and 0.5 M Na<sub>2</sub>SO<sub>4</sub> was the electrolyte solution; and we continued the UV irradiation. Fig. 9 shows that the photocurrent of TiO<sub>2</sub>-rGH and

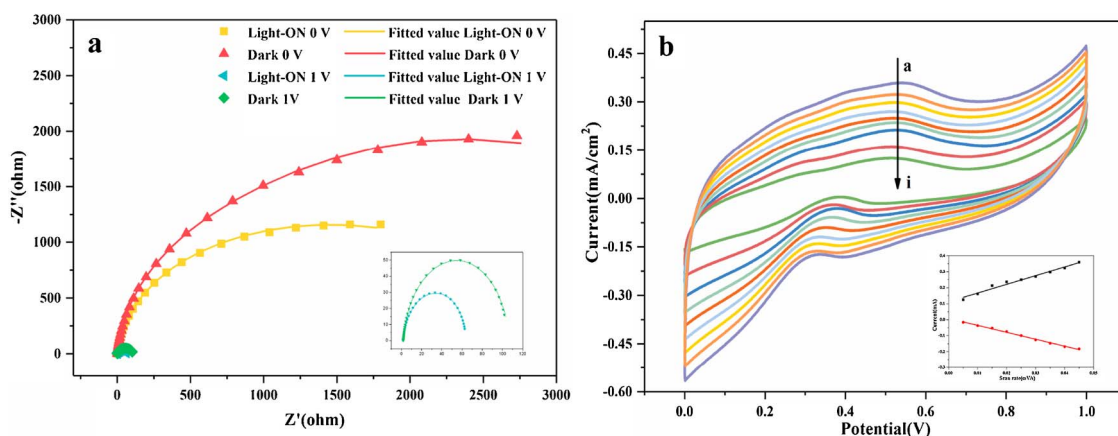


Fig. 8. (a) The influence of photo-irradiation and bias potential on the EIS, and (b) cyclic voltammograms of TiO<sub>2</sub>-rGH in 0.5 M Na<sub>2</sub>SO<sub>4</sub> containing 20 ppm BPA at various scan rates: 5, 10, 15, 20, 25, 30, 35, 40, and 45 mV/s. The inset represents the plots of the peak current versus scan rate.

**Table 1**  
EIS fitting data of the samples.

	R <sub>1</sub> (Ω)	R <sub>2</sub> (Ω)	R <sub>3</sub> (Ω)	CPE <sub>1</sub> (F)	CPE <sub>2</sub> (F)
Light-ON	1.745	0.1961	784.4	0.002269	0.003584
Dark	1.747	7.866	3308	0.003491	0.003692
Light-ON-1V	1.719	3.056	57.81	0.007255	0.001326
Dark-1V	1.759	2.846	99.12	0.008063	0.001236

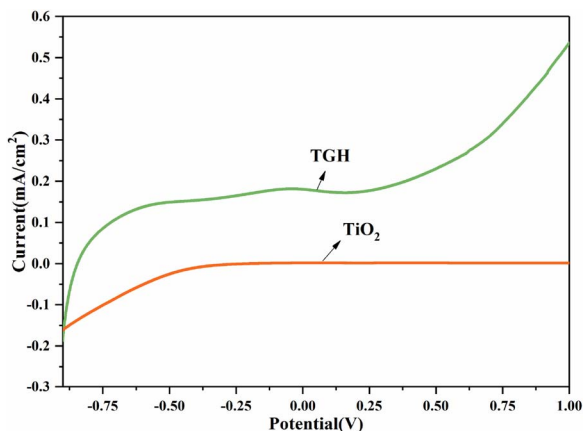


Fig. 9. Volt-ampere characteristic curve of  $\text{TiO}_2$  and  $\text{TiO}_2\text{-rGH}$ .

$\text{TiO}_2$  increases with an increase in voltage, but the  $\text{TiO}_2\text{-rGH}$  increases obviously. The photocurrent density of  $\text{TiO}_2$  is  $0.01 \text{ mA}/\text{cm}^2$  at the voltage of  $1 \text{ V}$ , which is due to the low charge transfer rate of  $\text{TiO}_2$  and the rapid recombination of electrons and holes. The photocurrent of  $\text{TiO}_2\text{-rGH}$  is up to  $0.52 \text{ mA}/\text{cm}^2$ , which proves that the presence of graphene promotes the separation of electron-hole pairs and accelerates the charge transfer rate, so the  $\text{TiO}_2\text{-rGH}$  has better PEC activity.

### 3.2. BPA adsorption performance of different types of photocatalysts

Adsorption equilibrium and adsorption kinetics are two important indexes to study the adsorption process. They can reflect the adsorption rate and adsorption capacity of the adsorbent. The adsorption capacity of  $\text{TiO}_2\text{-rGH}$  in different proportions is shown in Fig. 10a. We conducted adsorption experiments three times under the same conditions and obtained the average value. The content of rGH in  $\text{TiO}_2\text{-rGH}$  is the same. The data shows that the adsorption capacity of BPA increases abruptly in the initial stage of adsorption and then increases slowly. For about  $4 \text{ h}$ , all adsorbent materials reach the adsorption equilibrium. The solid line is calculated according to the quasi-second-order kinetics

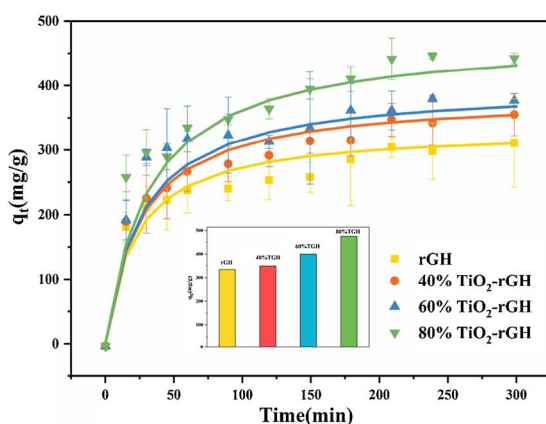


Fig. 10. (a) Effect of contact time on adsorption onto the different  $\text{TiO}_2\text{-rGHs}$ ; the inset represents BPA adsorption capacity of different  $\text{TiO}_2\text{-rGHs}$ . (b) Effect of contact time on adsorption onto the rGH, 80%  $\text{TiO}_2\text{-rGH}$ ,  $\text{TiO}_2\text{-AC}$ , and  $\text{TiO}_2\text{-rGO}$  thin film electrode.

model, and Table S1 gives the calculated results. The fitting results agree well with the experimental results, and the quasi-second-order kinetic model is ideal for fitting the experimental data. The correlation coefficient ( $R^2$ ) exceeds 0.99, and the theoretical calculated value of the adsorption equilibrium ( $q_{e,\text{cal}}$ ) is close to the experimental value ( $q_{e,\text{exp}}$ ). The deviation is within 2%, which indicates that the adsorption of BPA by  $\text{TiO}_2\text{-rGH}$  and rGH satisfies the quasi-second-order kinetic equation.

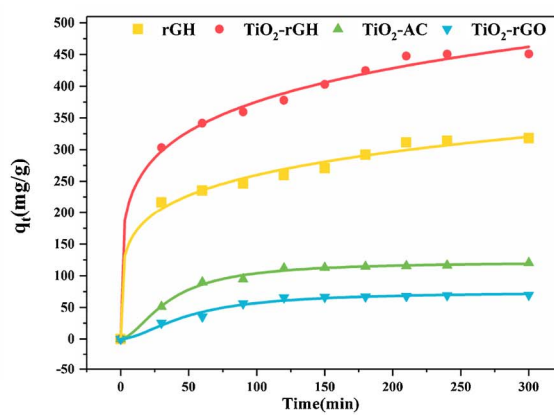
The inset of Fig. 10a suggests that an increase in the amount of  $\text{TiO}_2$  will open graphene pores resulting in an increase in the amount of saturated adsorption. The saturated adsorption capacity of 80%  $\text{TiO}_2\text{-rGH}$  is up to  $476.2 \text{ mg/g}$ , which is 1.4 times that of rGH ( $333.3 \text{ mg/g}$ ). As the  $\text{TiO}_2$  content increases, the adsorption capacity of graphene is mainly due to  $\pi\text{-}\pi$  conjugation [33]. Because the  $\text{TiO}_2$  holds up the graphene sheet, resulting in a thinner graphene sheet, the adsorption effect for BPA is more obvious.

Fig. 10b shows that the activated carbon and  $\text{TiO}_2$  composite enhances the limited adsorption capacity. The saturated adsorption capacity is  $120.3 \text{ mg/g}$ , although the saturated adsorption capacity of the  $\text{TiO}_2\text{-rGO}$  thin film electrode is only  $48.9 \text{ mg/g}$ . The adsorption capacity of the  $\text{TiO}_2\text{-rGO}$  thin film electrode is quite different from the saturated adsorption capacity of  $\text{TiO}_2\text{-rGH}$ . This is due to the small adsorption of BPA by the  $\pi\text{-}\pi$  conjugation, which only occurs on the graphene surface. The rGH can significantly improve the adsorption capacity of composite on BPA: the saturated adsorption capacity of  $476.2 \text{ mg/g}$  is 4.0 times that of  $\text{TiO}_2\text{-AC}$  and 9.7 times that of the  $\text{TiO}_2\text{-rGO}$  thin film electrode.

### 3.3. BPA removal by the combination of adsorption and photoelectrocatalysis of $\text{TiO}_2\text{-rGHs}$

Fig. 11a compares the PC, EC, and PEC degradation of  $\text{TiO}_2\text{-rGH}$  for BPA with  $4 \text{ h}$  of UV irradiation after adsorption equilibrium with a bias of  $1.5 \text{ V}$  and  $150 \text{ mg/L} \text{ Na}_2\text{SO}_4$  as the supporting electrolyte. The data show that PEC degradation of BPA is much higher than that of PC and EC degradation. After the adsorption equilibrium, the degradation rate of BPA is 25%, the PC degradation rate is 39%, the EC degradation rate is 42%, and the PEC degradation rate is nearly 100%. The effect of  $1 + 1 > 2$  is achieved proving that the applied bias voltage contributes to the transfer of charge and promotes the separation of electron-hole pairs, which is critical to the degradation effect.

Fig. 11b shows a  $C/C_0$  diagram of degradation of BPA by  $\text{TiO}_2\text{-rGH}$  adsorption, adsorption-photocatalysis, adsorption-electrocatalysis, and adsorption-photoelectrocatalysis. The bias voltage is  $1.5 \text{ V}$ , and  $150 \text{ mg/L} \text{ Na}_2\text{SO}_4$  is used to support the electrolyte. The figure shows that the adsorption rate of BPA is about 30% when the adsorption lasts about  $4 \text{ h}$ . When combined of adsorption and photocatalysis, the



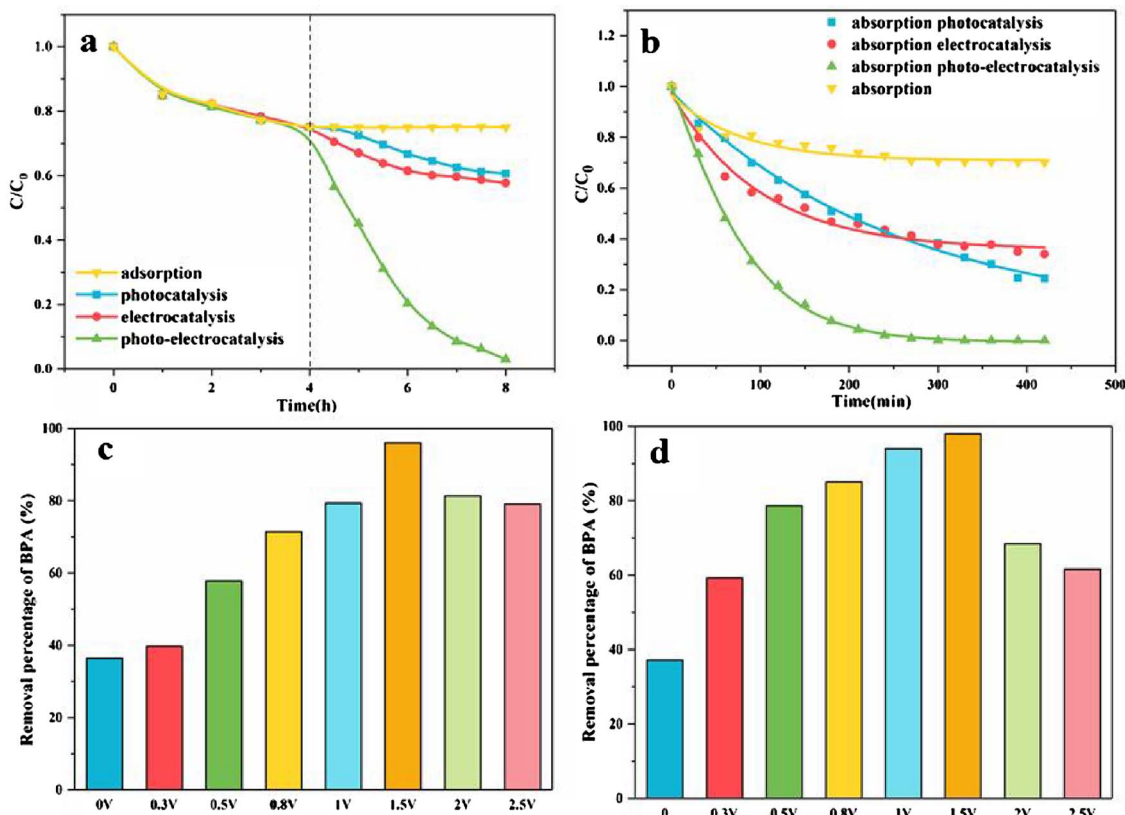


**Fig. 11.** (a) Comparison of PC, EC, and PEC activity of the  $\text{TiO}_2$ -rGH electrode decomposition of BPA. (b) Adsorption, adsorption-photocatalysis, adsorption-electrocatalysis, and adsorption-photoelectrocatalysis of BPA via  $\text{TiO}_2$ -rGH electrode. (c) The removal percentage of BPA under different bias conditions after adsorption equilibrium. (d) Adsorption-PEC degradation of BPA under different bias.

concentration decreases with time, and the degradation rate is 76%. Although the degradation rate of adsorption-electrocatalysis is higher than the initial adsorption-photocatalysis. This phenomenon is due to the higher initial concentration of BPA. The rapid adsorption of graphene leads to the synergistic degradation of BPA, which has an obvious effect. As the reaction progresses, organic matter continues to enrich the surface of the contaminated electrode, and it cannot maintain a high active state; therefore, the degradation efficiency of BPA decreased, and the degradation efficiency of BPA was 67% after 8 h of degradation.

Versus the previous two methods, the adsorption-photoelectrocatalysis degradation of BPA can achieve 100% degradation of BPA within 5 h. Fig. S1 shows that  $\ln(C/C_0)$  has a good linear relationship with time, and the rate constants during adsorption-photocatalysis degradation and adsorption-electrocatalysis degradation are rather similar, although the rate constant during adsorption-photoelectrocatalysis is much higher than the previous two methods. The rGH rapidly enriches the BPA to the inside and to the surface of the electrode. The addition of a certain bias can accelerate the charge conduction velocity, and thus the electrons produced by  $\text{TiO}_2$  with light are rapidly transferred to the counter electrode via the applied electric field and the graphene sheet.

The  $\text{TiO}_2$  exhibits extremely high PEC activity. When the bias voltage is higher than the decomposition voltage of water, water molecules on the surface of the photoelectron will be decomposed resulting in a large number of strong oxidizing substances such as  $\cdot\text{OH}$ . These phenomena are conducive to the decomposition of BPA. During adsorption-PEC degradation, the BPA can be fully and quickly mineralized. Therefore, this proves that this work offers a strategy to degrade pollutants. The adsorption-PEC degradation is clearly better.

To explore the effect of different external bias on the PEC degradation of BPA by photoelectrocatalysis, Fig. 11c shows that PEC

degradation was carried out for 4 h after 4 h adsorption equilibrium. In the absence of bias, the degradation efficiency was 37%, and the electrically-assisted PC phenomenon occurred when the bias voltage was 0.3 V. At this time, the degradation effect was improved to 40%, but the increase was not great. The voltage reached 0.5 V, and the solution began adsorption-PEC degradation. The effect of degradation at this time significantly improved to 58%. As the bias voltage increased to 1.5 V, the water molecules decomposed on the surface of the photoelectrode resulting in a large number of strong oxidizing substances such as  $\cdot\text{OH}$ . The presence of these substances can be further oxidized to BPA, which offers the best degradation effect. The degradation rate was 96% after 4 h UV irradiation. When the applied bias voltage reaches 2 V, the synergistic effect is reduced because of the competition between the decomposition of water on the surface of the photoelectrode and the degradation of the pollutants. The redistribution of the space charge layer and the Helmholtz layer decreases the number of carriers [17] and degradation efficiency. And high bias will lead to the production of large amounts of bubbles and other unfavorable hydrogel attached to the phenomenon of titanium wire [16]. Thus, the applied bias voltage of 1.5 V offers the best photoelectric effect. Fig. 11d shows the final degradation efficiency of adsorption-PEC degradation after 4 h UV irradiation. The degradation law is similar to that shown in Fig. 5c; 1.5 V is the best bias for adsorption-PEC degradation of BPA.

The comparison of BPA removal under different conditions after 5 h is shown in Fig. 12. Fig. 12a and b is the adsorption removal of BPA by rGH and  $\text{TiO}_2$ -rGH under dark reaction conditions, c and d are the removal rate of BPA over rGH and  $\text{TiO}_2$ -rGH under ultraviolet light respectively, e is the EC oxidation of BPA over  $\text{TiO}_2$ -rGH, and f is the PEC oxidation of BPA over  $\text{TiO}_2$ -rGH. The adsorption removal of BPA from 20.7% to 29.6% under dark reaction conditions in Fig. 12a and b. Our previous work [33] demonstrated that  $\text{TiO}_2$  nanoparticles were embedded on graphene sheets to inhibit the stacking of graphene sheets

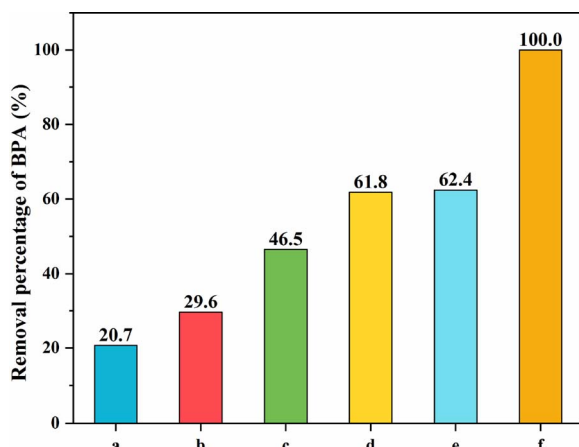


**Fig. 12.** The removal percentage of bisphenol A under different conditions, (a) adsorption over rGH, (b) adsorption over  $\text{TiO}_2$ -rGH, (c) rGH by UV irradiation, (d) adsorption-electrocatalysis over  $\text{TiO}_2$ -rGH, (e) adsorption-photocatalysis over  $\text{TiO}_2$ -rGH, (f) adsorption-photoelectrocatalysis over  $\text{TiO}_2$ -rGH.

and enhance the area of graphene sheets and then enhanced the  $\pi$ - $\pi$  conjugation and promoted the adsorption of BPA. A certain amount of degradation is also observed by the UV irradiation over rGH without  $\text{TiO}_2$  nanoparticles as shown in Fig. 12c, which could be explained by the direct photolysis of BPA in ultraviolet light [45]. As shown in Fig. 12d and e, the removal efficiency increases from 46.5% to 61.8% and 62.4% respectively after  $\text{TiO}_2$  nanoparticles was embedded onto rGH which indicates that electrocatalysis and photocatalysis could further increase the degradation of BPA. The 100% removal of BPA in Fig. 12f is due to the reason that the electrons produced by the  $\text{TiO}_2$  under UV irradiation are rapidly conducted to the counter electrode with the help of the electric field and the graphene sheet and the  $\text{TiO}_2$  exhibits a higher PC degradation activity. Furthermore, the bias voltage is higher than the decomposition voltage of water, water molecules in the surface of the electrode will be decomposed, resulting in a large number of strong oxidizing substances [48], which contributes to the decomposition of BPA adsorbed on the surface of graphene.

Fig. 13a compares the  $\text{TiO}_2$ -rGH with the  $\text{TiO}_2$ -rGO thin film electrode PEC degradation of BPA and shows that the degradation rate of BPA is 40% after 4 h of illumination of the  $\text{TiO}_2$ -rGO thin film electrode; the degradation rate of the  $\text{TiO}_2$ -rGH 3D electrode is as high as 96%. During the PEC reaction, it generally is believed that the following steps occur: the reactants are transferred to the surface of the electrode, the reactants adsorb on the electrode surface, the electrode reaction occurs, and the oxidation product from the electrode surface desorption and the electrode surface mass complete the transfer process. Many reports have suggested that adsorption is an important prerequisite for photocatalysis [46,47], and adsorption and electrode reactions are the most important steps in the PEC process. Therefore, the  $\text{TiO}_2$ -rGH can produce higher degradation than the  $\text{TiO}_2$ -rGO thin film. First, it depends on the structure of the inside and on the surface of the 3D electrode. The BPA is enriched on the surface and on the inside of the electrode, which is prerequisite for the subsequent high-speed degradation. Second,  $\text{TiO}_2$  nanoparticles on the surface of the  $\text{TiO}_2$ -rGO thin film electrode provide more catalytic activity sites, and the  $\text{TiO}_2$  nanoparticles are evenly distributed in the graphene layer. This results in improved inhibition of the light electron-hole pairs and improved catalytic capacity. In contrast to the  $\text{TiO}_2$ -rGH 3D electrode, the  $\text{TiO}_2$ -rGO film electrode showed better catalytic ability. Third, the  $\text{TiO}_2$  nanoparticles are distributed evenly on the inside and on the surface of the  $\text{TiO}_2$ -rGH 3D electrode and showed more catalytic active sites than the  $\text{TiO}_2$  nanoparticles agglomerated on the  $\text{TiO}_2$ -rGO thin film electrode. Finally, the  $\text{TiO}_2$  nanoparticles are evenly distributed on the graphene layer, which can better suppress the recombination of photogenerated electron-hole

pairs and improve catalytic ability. The  $\text{TiO}_2$ -rGH 3D electrode had better catalytic ability than the  $\text{TiO}_2$ -rGO thin film electrode. Fig. S2 shows the characteristic peaks of BPA appeared at the time of residence time of 5.0 min, and the characteristic peaks of BPA gradually decreased with an increase in irradiation time. The characteristic peak of BPA disappeared and the removal rate of BPA reached 100% at 5 h, which indicated that  $\text{TiO}_2$ -rGH had a good adsorption-PEC synergistic effect. Fig. 13b is a 3D HPLC before and after the BPA reaction of the  $\text{TiO}_2$ -rGH under UV irradiation. The figure shows that the characteristic peaks of BPA disappeared completely 5 h after the reaction. The degradation products of BPA during the PEC process were monitored by (HPLC-MS). As shown in Fig. S3, it can be concluded that the intermediate products of BPA is occurred within 180 min at 179.10 and 97.15  $m/z$ , and they may be aromatic compounds [48]. And the highest peak at this time was 56.2  $m/z$ , which proved that the product was a large number of ring-opening products (organic acids [49], etc.). After the reaction was carried out for 360 min, the bisphenol A peak disappeared completely. At this time, isopropylidene bridge cleavage takes place, leading to the formation of one ring hydroxylated phenolic derivatives at 195.05, and 157.15  $m/z$  [50]. In order to show the degree of mineralization at this time, we supplemented the TOC degradation rate experiment, the degradation rate of 82% TOC after 360 min, the degree of mineralization is higher than other similar literature [49].

Fig. 13c shows ability to recycle and regenerate the  $\text{TiO}_2$ -rGH. The  $\text{TiO}_2$ -rGH was subjected to 10 cycles of treatment, and the adsorption capacity of the  $\text{TiO}_2$ -rGH electrode is clearly attenuated. The efficiency of adsorption-PEC removal of BPA can approach 90%, which shows that the  $\text{TiO}_2$ -rGH has high catalytic capacity and self-regenerative ability. The  $\text{TiO}_2$ -rGH fixes the catalyst on the titanium wire mesh, which solves the shortcomings of the powder suspension catalytic system including its inability to inactivate and easily agglomerate as well as its complicated processing and high cost of the suspension.

ESR can detect free radicals in the reaction system [51]. Fig. 13d shows that no significant ESR signals are detected during dark reactions, but significant  $\cdot\text{O}_2^-$  and  $\cdot\text{OH}$  response signals are detected after light exposure. The electron transport mechanism of the  $\text{TiO}_2$ -rGH is shown in Fig. 14. During the process of adsorption-PEC degradation of BPA, adsorption and photoelectrocatalysis can promote and optimize each other and produce synergistic effects. Photoelectrocatalysis can not only eliminate the electrode's passivation effects due to adsorption of the phenolic polymer on the surface of the electrode, but can also promote adsorption resulting in adsorption-PEC degradation effects. When an appropriate bias potential is applied to the  $\text{TiO}_2$ -rGH, the photogenerated electrons are moved quickly and efficiently through the external circuit to the counter electrode (Pt electrode) under light irradiation. This charge transport process can reduce the photogenerated electrons and holes in the composite to improve degradation efficiency.

ESR analysis indicated that  $\cdot\text{O}_2^-$  and  $\cdot\text{OH}$  are the main active species involved in the degradation of BPA and its oxidized intermediates. These results suggest that efficient catalytic mineralization of the  $\text{TiO}_2$ -rGH mainly results from the synergistic effects between adsorption enrichment and in situ PEC oxidation. Based on the above results and discussion, the efficient PEC mineralization ability of  $\text{TiO}_2$ -rGH should mainly benefit from the synergism between adsorption-enrichment and in-situ PEC oxidation. Therefore, we propose the PEC mechanism of  $\text{TiO}_2$ -rGH. Using the combination of ultraviolet light and electric field, many  $\cdot\text{OH}$  and  $\cdot\text{O}_2^-$  free radicals are generated in the  $\text{TiO}_2$ -rGH surface to effectively oxidize organic pollutants for  $\text{CO}_2$  and  $\text{H}_2\text{O}$ .

#### 4. Conclusion

We synthesized a  $\text{TiO}_2$ -rGH with a 3D network structure with highly efficient photoelectrocatalytic degradation enriched by adsorption. The  $\text{TiO}_2$ -rGH electrode has a good adsorption effect, a saturated adsorption

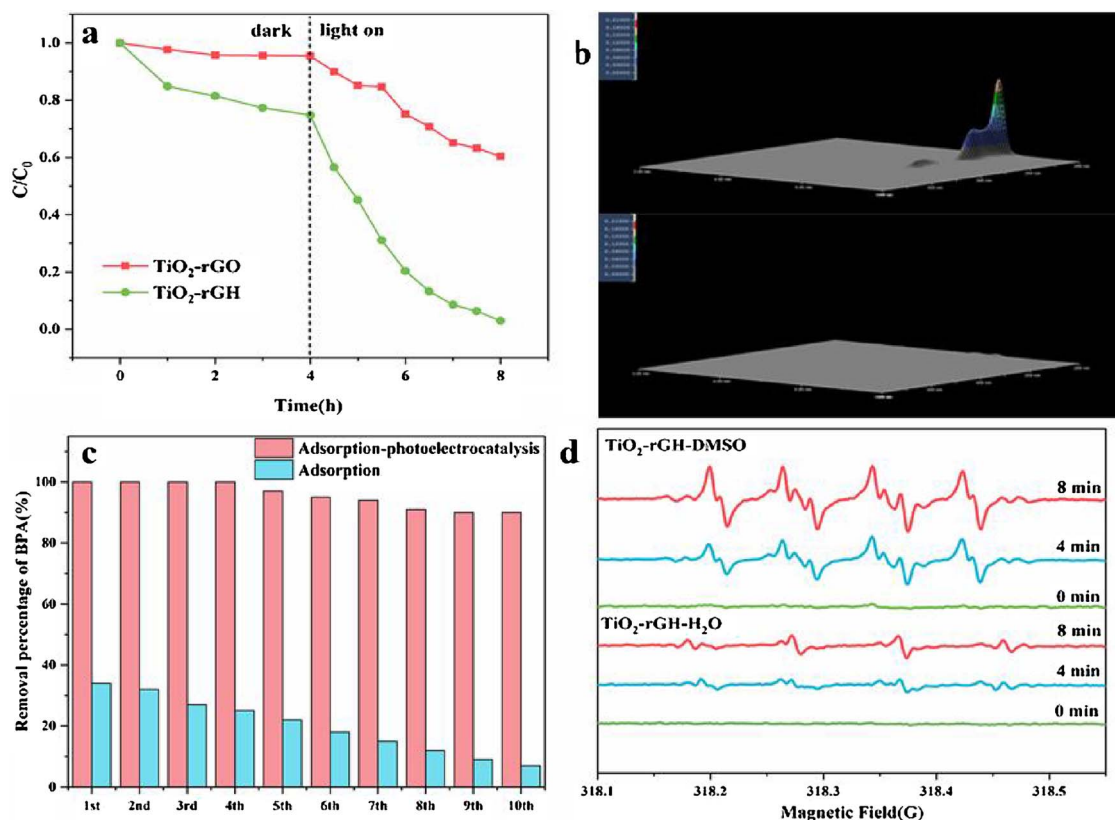


Fig. 13. (a)  $\text{TiO}_2\text{-rGH}$  electrode with  $\text{TiO}_2\text{-rGO}$  thin film electrode photoelectric degradation of BPA. (b) 3D HPLC of BPA solution before and after degradation of the  $\text{TiO}_2\text{-rGH}$  electrode. (c) Cycle runs of the TGH for removal of BPA under the absorption-photocatalysis. (d) DMPO spin-trapping ESR spectra of TGH in DMSO and water.

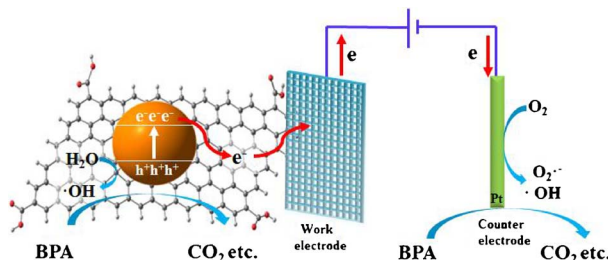


Fig. 14. Schematic diagrams for the electron transfer in the TGH and the PEC degradation mechanism of BPA under UV irradiation.

capacity of 476.2 mg/g, 4.0 times that of  $\text{TiO}_2\text{-AC}$ , and 9.7 times that of the  $\text{TiO}_2\text{-rGO}$  film electrode. The  $\text{TiO}_2\text{-rGH}$  has the combination of high-efficiency adsorption and in situ rapid PEC degradation, and the removal rate of low-concentration BPA (20 mg/L) is as high as 100% at 5 h. In contrast, the BPA degradation of the  $\text{TiO}_2\text{-rGO}$  thin film electrode was 40% after 4 h of UV irradiation, but the removal rate of BPA over the same mass of the  $\text{TiO}_2\text{-rGH}$  electrode had a rate up to 96%. At the same time, by recycling the  $\text{TiO}_2\text{-rGH}$  electrode special macroscopic hydrogel mesh structure 10 times, the removal rate of BPA could be maintained at more than 90%. The PEC activity of  $\text{TiO}_2\text{-rGH}$  3D electrode was better than that of the  $\text{TiO}_2\text{-rGO}$  thin film electrode. The cycling capacity and self-regenerative ability of the  $\text{TiO}_2\text{-rGH}$  indicating superiority of separation freely without filter system for 3D structured hydrogel. The results show that the  $\text{TiO}_2\text{-rGH}$  not only has good separation and recovery characteristics, but also exhibits excellent adsorption-PEC ability. Owing to their remarkable features, it is expected that the strategy used in this work may be used to fabricate other functional hydrogel for water purification.

## Acknowledgments

This work was financially supported by the National Natural Science Foundation of China (No. 51672081), Key Program of Natural Science of Hebei Province (B2016209375), Hebei Provincial Foundation for International cooperation (15391403D).

## Appendix A. Supplementary data

Supplementary data associated with this article can be found, in the online version, at <http://dx.doi.org/10.1016/j.apcatb.2017.08.076>.

## References

- [1] J.E. Casillas, F. Tzompantzi, S.G. Castellanos, G. Mendoza-Damián, R. Pérez-Hernández, A. López-Gaona, A. Barreraa, *Appl. Catal. B* 208 (2017) 161–170.
- [2] S. Li, G. Zhang, P. Wang, H. Zheng, Y. Zheng, *Chem. Eng. J.* 294 (2016) 371–379.
- [3] W.Q. Cui, W.J. An, L. Liu, J. Hu, Y. Liang, *J. Hazard. Mater.* 280 (2014) 417–427.
- [4] H.P. Cong, X.C. Ren, P. Wang, S.H. Yu, *ACS Nano* 6 (2012) 2693–2703.
- [5] G.C.J. Jou, *Carbon* 36 (1998) 1643–1648.
- [6] Y. Lei, F. Chen, Y. Luo, L. Zhang, *J. Mater. Sci.* 49 (2014) 4236–4245.
- [7] D. Zhang, B. Pan, H. Zhang, P. Ning, B. Xing, *Environ. Sci. Technol.* 44 (2010) 3806–3811.
- [8] W. Ren, D. Tang, X. Lu, J. Sun, M. Li, S. Qiu, D. Fan, *Ind. Eng. Chem. Fundam.* 55 (2016) 11085–11096.
- [9] D. Wang, J. Wang, Z. Liu, X. Yang, X. Hu, J. Deng, N. Yang, Q. Wang, Q. Yuan, *ACS Appl. Mater. Interfaces* 8 (2015) 28265–28273.
- [10] A. Fujishima, *Nature* 238 (1972) 37–38.
- [11] C. Acar, I. Dincer, G.F. Naterer, *Int. J. Energy Res.* 40 (2016) 1449–1473.
- [12] V. Etacheri, C. Di Valentin, J. Schneider, D. Bahnemann, S.C. Pillai, *J. Photochem. Photobiol. C* 25 (2015) 1–29.
- [13] C. Dette, M.A. Pérez-Osorio, C.S. Kley, P. Punke, C.E. Patrick, P. Jacobson, F. Giustino, S. Jung, K. Kern, *Nano Lett.* 14 (2014) 6533–6538.
- [14] D. Kang, T.W. Kim, S.R. Kubota, A.C. Cardiel, H.G. Cha, K.S. Choi, *Chem. Rev.* 115 (2015) 12839–12887.
- [15] X.P. Chen, Z.X. Zhang, L. Chi, A.K. Nair, W.F. Shangguan, Z. Jiang, *Nano-Micro Lett.* 8 (2016) 1–12.
- [16] Z. Frontistis, V.M. Daskalaki, A. Katsaounis, I. Poulios, D. Mantzavinos, *Water Res.* 45 (2011) 2996–3004.

[17] Z. Wei, F. Liang, Y. Liu, W. Luo, J. Wang, W. Yao, Y.F. Zhu, *Appl. Catal. B* 201 (2017) 600–606.

[18] Y. Liang, Z.C. Guan, H.P. Wang, R.G. Du, *Electrochem. Commun.* 77 (2017) 120–123.

[19] M. Hamandi, G. Berhault, C. Guillard, H. Kochkar, *Appl. Catal. B* 209 (2017) 203–213.

[20] M.D. Stoller, S. Park, Y. Zhu, J. An, R.S. Ruoff, *Nano Lett.* 8 (2008) 3498–3502.

[21] K.I. Bolotin, K.J. Sikes, Z. Jiang, M. Klima, G. Fudenberg, J. Hone, P. Kim, H.L. Stormer, *Solid State Commun.* 146 (2008) 351–355.

[22] C. Lee, X. Wei, J.W. Kysar, J. Hone, *Science* 321 (2008) 385–388.

[23] R.R. Nair, P. Blake, A.N. Grigorenko, K.S. Novoselov, T.J. Booth, T. Stauber, A.K. Geim, *Science* 320 (2008) 1308.

[24] W. Chen, J. Ni, J. Hazard. Mater. 324 (2017) 321–328.

[25] J.G. Martinez, S. Aznar-Cervantes, A.A. Lozano-Pérez, J.L. Cenís, T.F. Otero, *Electrochim. Acta* 209 (2016) 521–528.

[26] Y.C. Pu, H.Y. Chou, W.S. Kuo, K.H. Wei, Y.J. Hsu, *Appl. Catal. B* 204 (2017) 21–32.

[27] H. Moussa, E. Girot, K. Mozet, H. Alem, G. Medjahdi, R. Schneider, *Appl. Catal. B* 185 (2016) 11–21.

[28] J. Di, J. Xia, H. Li, Z. Liu, *Nano Energy* 35 (2017) 79–91.

[29] Z. Fan, J. Yan, L. Zhi, Q. Zhang, T. Wei, J. Feng, F. Wei, *Adv. Mater.* 22 (2010) 3723–3728.

[30] H. Choi, H. Kim, S. Hwang, M. Kang, D.W. Jung, M. Jeon, *Scr. Mater.* 64 (2011) 601–604.

[31] H. Wang, X. Yuan, G. Zeng, Y. Wu, Y. Liu, Q. Jiang, S. Gu, *Adv. Colloid Interface Sci.* 221 (2015) 41–59.

[32] Z. Zhang, F. Xiao, Y. Guo, S. Wang, Y. Liu, *ACS Appl. Mater. Interfaces* 5 (2013) 2227–2233.

[33] Y. Li, W. Cui, L. Liu, R. Zong, W. Yao, Y. Liang, Y. Zhu, *Appl. Catal. B* 199 (2016) 412–423.

[34] S. Anandan, T.N. Rao, M. Sathish, D. Rangappa, I. Honma, M. Miyauchi, *ACS Appl. Mater. Interfaces* 5 (2013) 207–212.

[35] H. Wang, C. Guan, X. Wang, H.J. Fan, *Small* 11 (2015) 1470–1477.

[36] A.V. Murugan, T. Muraliganth, A. Manthiram, *Rapid Chem. Mater.* 21 (2009) 5004–5006.

[37] J. Xu, L. Wang, Y.F. Zhu, *Langmuir* 28 (2012) 8418–8425.

[38] Y. Zhang, X. Hou, T. Sun, X. Zhao, *Ceram. Int.* 43 (2017) 1150–1159.

[39] A.C. Ferrari, J.C. Meyer, V. Scardaci, C. Casiraghi, M. Lazzari, F. Mauri, A.K. Geim, *Phys. Rev. Lett.* 97 (2006) 187401.

[40] K. Ai, Y. Liu, L. Lu, X. Cheng, L. Huo, *J. Mater. Chem.* 21 (2011) 3365–3370.

[41] X. Pan, Y. Zhao, S. Liu, C.L. Korzeniewski, S. Wang, Z. Fan, *ACS Appl. Mater. Interfaces* 4 (2012) 3944–3950.

[42] H.M. Zhao, F. Su, X.F. Fan, H.T. Yu, D. Wu, X. Quan, *Chin. J. Catal.* 33 (2012) 777–782.

[43] J. Xiang, Z.G. Liu, J.H. Ouyang, Y. Zhou, F.Y. Yan, *Solid State Ionics* 220 (2012) 7–11.

[44] Y.M. Jiang, L.P. Jia, S.J. Yu, C.M. Wang, *J. Mater. Chem. A* 2 (18) (2014) 6656–6662.

[45] H. Katsumata, S. Kawabe, S. Kaneko, T. Suzuki, K. Ohta, *J. Photochem. Photobiol. A* 162 (2) (2004) 297–305.

[46] Y.H. Hsien, C.F. Chang, Y.H. Chen, S. Cheng, *Appl. Catal. B* 31 (2001) 241–249.

[47] H. Liu, X.Z. Li, Y.J. Leng, W.Z. Li, *J. Phys. Chem. B* 107 (2003) 8988–8996.

[48] D. Subagio, M. Srinivasan, M. Lim, T. Lim, *Appl. Catal. B* 95 (2010) 414–422.

[49] C. Chang, Y. Fu, M. Hu, C. Wang, G. Shan, L. Zhu, *Appl. Catal. B* 142–143 (2013) 553–560.

[50] A.R. Bakr, M.S. Rahaman, *Chemosphere* 185 (2017) 879–887.

[51] F.F. Liang, Y.F. Zhu, *Appl. Catal. B* 180 (2016) 324–329.